Reaction of (N4Py)Fe with H_2O_2 and the relevance of its Fe(IV)=O species during and after H_2O_2 disproportionation

de Roo, C. Maurits; Sardjan, Andy S.; Postmus, Roy; Swart, Marcel; Hage, Ronald; Browne, Wesley R.

Published in:
ChemCatChem

DOI:
10.1002/cctc.202301594

Publication date:
2024

ChemCatChem

Research Article
doi.org/10.1002/cctc.202301594

Chemistry Europe
European Chemical Societies Publishing

www.chemcatchem.org

Reaction of (N4Py)Fe with H_2O_2 and the relevance of its Fe(IV) = O species during and after H_2O_2 disproportionation

C. Maurits de Roo,[a] Andy S. Sardjan,[a] Roy Postmus,[a] Marcel Swart,[b, c] Ronald Hage,*[a] and Wesley R. Browne*[a]

The catalytic disproportionation of by non-heme Fe(II) complexes of H_2O_2 the ligand N4Py (1,1-bis(pyridin-2-yl)-*N*,*N*-bis(pyridin-2-ylmethyl)methanamine) and the formation and reactivity of Fe(III)-OOH and Fe(IV) = O species is studied by UV/Vis absorption, NIR luminescence, (resonance) Raman and headspace Raman spectroscopy, $^1O_2$ trapping and DFT methods. Earlier DFT studies indicated that disproportionation of H_2O_2 catalysed by Fe(II)-N4Py complexes produce only $^3O_2$, however, only the low-spin state pathway was considered. In the present study, DFT calculations predict two pathways for the reaction between Fe(III)-OOH and H_2O_2, both of which yield $^3O_2/H_2O_2$ and involve either the $S = 1/2$ or the $S = 3/2$ spin state, with the latter being spin forbidden. The driving force for both pathways are similar, however, a minimal energy crossing point (MECP) provides a route for the formally spin forbidden reaction. The energy gap between the reaction intermediate and the MECP is lower than the barrier across the non-adiabatic channel. The formation of $^3O_2$ only is confirmed experimentally in the present study through $^1O_2$ trapping and NIR luminescence spectroscopy. However, attempts to use the $^1O_2$ probe (α-terpinene) resulted in initiation of auto-oxidation rather than formation of the expected endoperoxide, which indicated formation of OH radicals from Fe(III)-OOH, *e.g.*, through O–O bond homolysis together with saturation of methanol with $^3O_2$. Microkinetic modelling of spectroscopic data using rate constants determined earlier, reveal that there is another pathway for Fe(III)-OOH decomposition in addition to competition between the reaction of Fe(III)-OOH with H_2O_2 and homolysis to form Fe(IV) = O and hydroxyl radical. Notably, after all H_2O_2 is consumed the decay of the Fe(III)-OOH species is predominantly through a second order self reaction (with Fe(III)-OOH). The conclusion reached is that the rate of O–O bond homolysis in the Fe(III)-OOH species to form Fe(IV) = O and an hydroxyl radical is too low to be responsible for the observed oxidation of organic substrates.

Introduction

H_2O_2 is a widely used terminal oxidant in organic transformations since it is kinetically stable, despite being a'high energy' reagent, and is atom efficient with only O_2 and H_2O as by-products. The decomposition of H_2O_2 is an important process in biology, and nature has evolved mechanisms to deactivate it without production of reactive oxygen species.[1] At low concentrations of H_2O_2, oxidases operate effectively with two-electron reductants, in much the same way as H_2O_2 is used as an oxidant in transition metal catalysed reactions through generation of reactive species that are then used to oxidise organic substrates.[2] At high concentrations of H_2O_2 its role as a substrate for these same species can be observed and is indeed how organisms deal with H_2O_2 under those circumstances, through enzyme catalysed disproportionation of H_2O_2 to O_2 and water (*i.e.* catalases).[3] The active center of these enzymes typically includes a transition metal center, *e.g.*, a heme iron center that reacts with H_2O_2 by heterolytic cleavage of the O–O bond to form an Fe(IV) = O species (Compound I) and water.[3] Although this deactivates one molecule of H_2O_2, the resulting high valent species can engage in one or two-electron oxidation of substrates, including H_2O_2 to liberate O_2, recovering the initial state. Enzymatic deactivation of H_2O_2 generally seeks to avoid production of reactive oxygen species such as hydroxyl radicals and $^1O_2$. Replicating this selectivity is a challenge in biomimetic systems where the focus is typically to harness the oxidising power of H_2O_2 towards oxidation of organic substrates.

In contrast to iron dependent catalases, synthetic non-heme iron complexes based on pyridyl-amine based ligands, such as TPA, BPMEN, and N4Py (Figure 1), and indeed the antibiotic Fe-Bleomycin, rapidly undergo ligand exchange and/or oxidation reactions to reach a meta-stable Fe(III)-OOH species, which are proposed to form Fe(IV) = O species through homolytic cleavage of the O–O bond.[4,5] It is these latter species that are

[a] *C. Maurits de Roo0009-0004-1493-9809, A. S. Sardjan, R. Postmus, Prof. Dr. R. Hage, Prof. Dr. W. R. Browne*
Stratingh Institute for Chemistry, Faculty of Science and Engineering, University of Groningen, Nijenborgh 4, 9747AG, Groningen, The Netherlands
E-mail: r.hage@rug.nl
w.r.browne@rug.nl
Homepage: 0009-0004-1493-9809

[b] *Prof. Dr. M. Swart*
IQCC and Department of Chemistry, Universitat de Girona, ParcUdG, c/ Emili Grahit 91, 17003, Girona, Spain

[c] *Prof. Dr. M. Swart*
ICREA, Pg. Lluís Companys 23, 08010 Barcelona, Spain

Supporting information for this article is available on the WWW under https://doi.org/10.1002/cctc.202301594

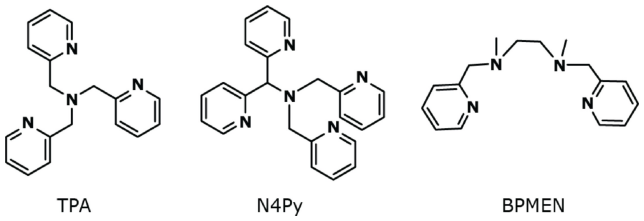

Figure 1. Structures of the ligands TPA, N4Py, and BPMEN.

deemed responsible for the oxidation of organic substrates.[6,7] This paradigm mechanism has recently shown exceptions, such as in the (transient) formation of Fe(V)=O species,[8,9] in the direct dihydroxylation of alkenes with Fe(III)-OOH species reported recently by the Nam group,[10] and in olefin epoxidation and alkene hydroxylation with a diferric peroxo intermediate reported by the Que group.[11] Additionally, control of the formation of either Fe(IV)=O or Fe(III)-OOH species using a phenol-bearing ligand and base was reported by the Banse group.[12,13]

Recently, we reported[14] that the complex $[Fe(II)(N_4Py)(CH_3CN)]^{2+}$ (**1**), where N4Py is 1,1-bis(pyridin-2-yl)-*N*,*N*-bis(pyridin-2-ylmethyl)methanamine),[4,5,15,16] was an effective catalyst for the disproportionation of H_2O_2 into O_2 and H_2O in methanol. **1** undergoes solvolysis in methanol to form $[Fe(II)(N_4Py)(OCH_3)]^{+}$ (**2**) and upon addition of H_2O_2 rapidly forms $[Fe(III)(N_4Py)(OOH)]^{2+}$ (**3**). We demonstrated that while the homolytic cleavage of the O–O bond in to yield an Fe(IV)=O species (**4**) is generally assumed, this last process (Figure 2 pathway b) is not kinetically competent and instead H_2O_2 reacts directly with **3** to form $[Fe(III)(N_4Py)(OCH_3)]^{2+}$ (**5a**), H_2O and O_2, (Figure 2 pathway a). DFT calculations indicated that O_2 was formed as $^3O_2$ in a $S=\frac{1}{2}$ state that results from two unpaired electrons on $^3O_2$ ($m_s=1$) coupled to one unpaired electron on iron ($m_s=-\frac{1}{2}$). Nevertheless, the formation of $^1O_2$ should be excluded experimentally due to the latter's ability to initiate undesirable reactions. Disproportionation of H_2O_2 is undesirable in the context of catalytic oxidations of organic substrates due to its impact on efficiency, and a common approach is to use a low steady state concentration of H_2O_2 to increase atom efficiency. Such an approach appeared to be effective in regard to the oxidation of methanol to methanal by H_2O_2 and **1**.[14] However, the generation of reactive oxygen species, not least hydroxyl radicals and $^1O_2$ can impact selectivity, or in the case of $^1O_2$, enable new reactions with H_2O_2.

In the present contribution we focus on the mechanism by which **3** reacts with H_2O_2. The possible generation of $^1O_2$ and the rate constant for homolysis of the O–O bond of **3** are investigated. Two approaches, a chemical probe and chemiluminescence, were taken to establish whether or not $^1O_2$ is formed during disproportionation. We revisit the DFT studies by considering minimum energy crossing points (MECPs) between the doublet and quartet surfaces. Furthermore, we use a microkinetic model based on the mechanism described in Figure 2 to establish the significance of pathway b (O–O bond homolysis) overall and thereby the origin of oxidation products of methanol.

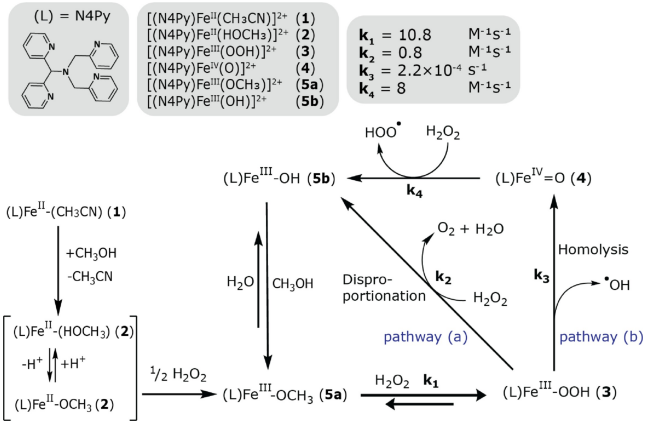

Figure 2. Proposed mechanism for reaction of **1** with excess H_2O_2 in methanol.

Results

The decomposition of H_2O_2 to water and oxygen by **1** was studied earlier by solution and head space Raman spectroscopy,[14] where a discrepancy in mass balance was noted (see SI section 1 experimental section for details). The decomposition is revisited here to establish a full mass balance in the disproportionation reaction before addressing experimentally and theoretically the spin state of the O_2 produced, and finally kinetic analyses to build a microkinetic model for the reaction.

O_2 release during decomposition of H_2O_2 by 1

In line monitoring of both the headspace and reaction mixture with Raman spectroscopy allows for simultaneous quantitative comparison of the extent of consumption of H_2O_2 and the amount of $^3O_2$ released into the head space (Figure 3). It should be noted, in regard to discussion below, that even were $^1O_2$ to be formed during the reaction, it relaxes to $^3O_2$ within ca. 9.5 μs of formation,[17,18] and hence the operando Raman spectroscopy cannot be used for (dis)proving the presence of $^1O_2$ as one of the products in the reaction. The amount of $^3O_2$ liberated, calculated from the change in intensity of the Raman band of $^3O_2$ (*i.e.*the $\tilde{\nu}_{str,OO}$ band at 1555 cm^{-1}, Figure 3A), can be compared directly with the decrease in intensity of the $\tilde{\nu}_{str,OO}$ band of H_2O_2 at 872 cm^{-1} (Figure 3B) in the reaction mixture, and from which the absolute amounts of $^3O_2$ formed and H_2O_2 consumed over time can be determined (Figure 3C, see SI section 1 for determination of $^3O_2$ concentration, Figures S1–4). Although a full mass balance is obtained towards the end of the reaction and the decomposition of H_2O_2 over time shows the expected pseudo-first order behavior, the increase in concentration of O_2 in the headspace appears to lag that of consumption of H_2O_2. This delay in response is likely a consequence of the experimental conditions as the solution

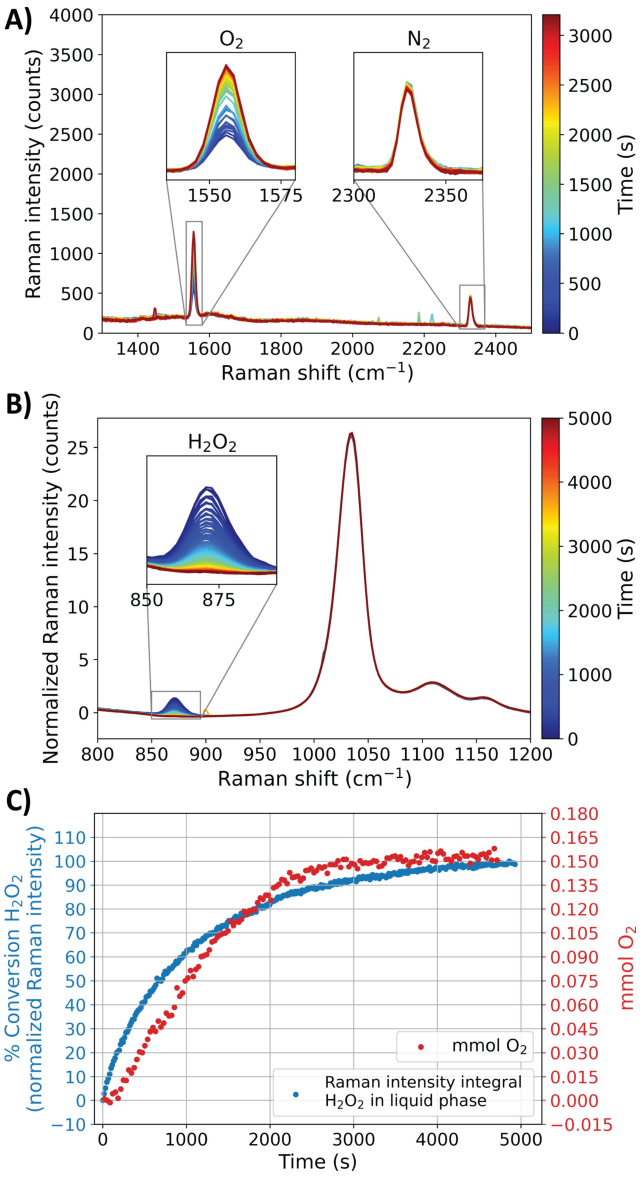

Figure 3. Decomposition of H_2O_2 catalysed by **1** in methanol. A) Head space Raman spectra (λ_{exc} 785 nm) over time. The $^3O_2$ and N_2 bands are shown as insets. B) Raman spectra (λ_{exc} 785 nm) of the reaction mixture. The $\tilde{\nu}_{str,OO}$ band of H_2O_2 is shown as an inset. C) Conversion of H_2O_2 and amount of $^3O_2$ formed over time. Conditions: 0.5 mM **1**, 200 mM H_2O_2 in 1.5 mL MeOH.

was not stirred during the reaction, and hence due in small part to the delay reaching saturation of the methanol in O_2 and the build up of bubbles of oxygen in the solution and in part due to lack of convective forces. Experiments with the photosensitiser $[Ru(II)(bipy)_3](PF_6)_2$, *vide infra*, confirm that the solution is saturated in oxygen rapidly after addition of H_2O_2. Although the evolution of $^3O_2$ can be determined readily by head space Raman spectroscopy, detecting $^1O_2$ formed is more challenging and indirect methods ($^1O_2$ trapping) were employed.

Trapping of $^1O_2$ with α-terpinene

α-terpinene is a widely used probe for determining formation of $^1O_2$ in solution,[19–21] as the latter is a dienophile in a cycloaddition to form the endoperoxide ascaridole (Figure 4A). The disproportionation of excess H_2O_2 was followed by Raman spectroscopy (both liquid phase and head space) in the presence of α-terpinene (Figure 5, and Figure S5). Under these reaction conditions 22% of the α-terpinene was converted to another compound within 1 h. However, rather than increasing, the Raman band of $^3O_2$ in the head space spectrum decreased over the course of the reaction also (Figure 6). Comparison of the intensity of the $\tilde{\nu}_{C=C}$ band of α-terpinene and the O–O stretch of $^3O_2$ over time shows that the amount of $^3O_2$ in the head space increases slightly in the first few hundred seconds

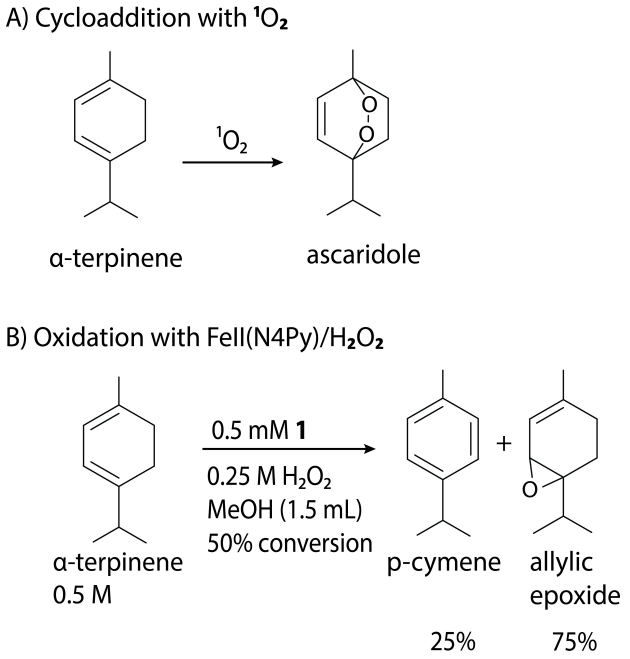

Figure 4. A) Cycloaddition of $^1O_2$ to α-terpinene yielding an endoperoxide (ascaridole). B) Observed oxidation of α-terpinene with the **1**/H_2O_2 system. 0.52 mM **1**, 0.25 M H_2O_2, and 0.5 M α-terpinene in methanol at 19 °C.

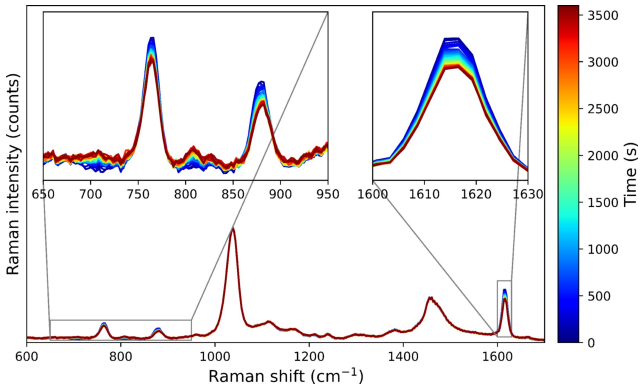

Figure 5. Raman spectra (λ_{exc} 1064 nm) over 1 h of the reaction of α-terpinene in methanol with H_2O_2 and **1**. See Figure S7 for the corresponding head space Raman spectra. Conditions: 0.5 mM **1**, 165 mM H_2O_2 and 0.5 M α-terpinene in methanol at 19 °C.

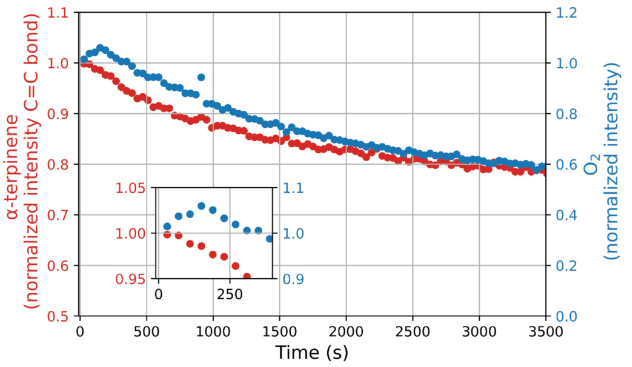

Mass balance analysis:

0.165 mmol α-terpinene converted (= 22%) = 0.041 mmol O_2 withdrawn from the head space + 0.123 mmol O_2 originating from H_2O_2 disproportionation

Figure 6. Normalized Raman intensity over time of the $\nu_{str,C=C}$ band of α-terpinene (red) and the $\nu_{O=O}$ band of $^3O_2$ (blue, recorded from the head space). Mass balance analysis shows that the amount of converted α-terpinene equals the total amount of converted $^3O_2$. Conditions: 0.5 mM **1**, 165 mM H_2O_2 and 0.5 M α-terpinene in methanol at 19 °C.

(inset of Figure 6), as expected due to disproportionation of H_2O_2, but thereafter decreases to approximately half of its original amount, i.e., $^3O_2$ was consumed from head space. In contrast, the intensity of the $\tilde{\nu}_{C=C}$ band of α-terpinene is unchanged over the initial period (lag time) and only thereafter is conversion observed, which tracks closely the loss of $^3O_2$ from the headspace. Quantification of $^3O_2$ in the head space indicates that the $^3O_2$ that is consumed from the head space (0.041 mmol) corresponds to the difference between the amount of α-terpinene converted (0.165 mmol) and the amount of $^3O_2$ expected to be liberated by H_2O_2 disproportionation (0.123 mmol, i.e., 165 mM H_2O_2 in a 1.5 mL reaction mixture gives 0.247 mmol H_2O_2. Considering that two molecules of H_2O_2 result into one molecule of $^3O_2$; 0.247/2 = 0.123 mmol $^3O_2$). Hence, the conversion of α-terpinene is the sum of the $^3O_2$ produced from H_2O_2 and $^3O_2$ consumed from the head space. This correlation indicates that α-terpinene is reacting with $^3O_2$ rather than any $^1O_2$ that would be formed during H_2O_2 decomposition. Indeed, analysis by ^{1}H-NMR and Raman spectroscopy confirms the formation of *p*-cymene as the primary product (Figures 4B, S5, and note Raman bands that appear at around 700 and 810 cm^{-1} in Figure 5). This is consistent with α-terpinene engaging in auto-oxidation (Figure S6),[22] initiated by radicals and either reacts with $^3O_2$ to form an aromatic product, *p*-cymene, or reacts with hydroperoxyl radicals (formed during formation of *p*-cymene), to yield allylic epoxides (see SI section 2 for further details).

Consideration of the disproportionation of H_2O_2, at high concentrations, by **1**, allows for rationalisation of why α-terpinene shows auto-oxidation with the H_2O_2/**1**-system (Figure 2 pathway b). Several radical intermediates or radical sources appear in the proposed mechanism and although pathway (b) is unfavourable, radical abstraction by an hydroxyl radical or **4** can initiate radical auto-oxidation. Although, **1** is ultimately responsible for initiating auto-oxidation (conversion is not observed in the absence of **1**, Figure S7), the short lag period implies that the increase in the concentration of O_2 in solution plays a role also.

The generation of $^1O_2$ from H_2O_2 using MoO_4^{2-} as catalyst was studied extensively by Aubry et al.[23–28] Although the mechanism of the reaction is complex (*e.g.*, concentration dependent equilibria involving several peroxomolybdate species dependent on [H_2O_2]), it has been used in large scale (batch) reactions,[28] as a heterogeneous catalyst by immobilization of the molybdate,[29] and in flow reactors.[30] Hence, as a positive control in the present study α-terpinene was reacted with $^1O_2$ generated with $MoO4^{2-}$.[31,32] Raman spectra recorded over time and ^{1}H-NMR spectra before and after the oxidation of α-terpinene in the presence of Li_2MoO_4 catalyst and H_2O_2 (Figures S8 and S9) show the expected ascaridole product. Hence, the susceptibility of chemical probes for $^1O_2$ to other oxidation mechanisms that can be initiated during catalytic decomposition of H_2O_2 means that it cannot be concluded that $^1O_2$ is not formed by decomposition of H_2O_2 by **1**. Hence the direct observation of $^1O_2$ by chemiluminescence was explored.

$^1O_2$ chemiluminescence with MoO_4^{2-}

Regardless of whether $^1O_2$ is generated by photosensitisation, using, *e.g.*, Rose bengal, or by thermal decomposition of another compound,*e.g.*, the disproportionation of H_2O_2 or thermal decomposition of an endoperoxide, $^1O_2$ relaxes rapidly to $^3O_2$ either non-radiatively, or radiatively with emission in the NIR (1270 nm). Detection of the weak chemiluminescence of $^1O_2$ is challenging due to the low photon flux. Hence, the decomposition of H_2O_2 to $^1O_2$ and water by the catalyst Li_2MoO_4, which proceeds with unit chemical efficiency, was used as a positive control.[23–27] The rate of H_2O_2 disproportionation by the catalysts was determined using simultaneous head space Raman spectroscopy (to determine $^3O_2$ released) and the NIR emission from the $^1O_2$ produced. This combination of techniques allowed us to apply conditions where the rate of disproprotionation by **1** exceeds that of the Li_2MoO_4 / H_2O_2 system. As for the reaction of **1** with H_2O_2 (Figure 3), the reaction of Li_2MoO_4 with H_2O_2 was monitored by head space and solution Raman spectroscopy (Figure S10).

The mechanism of disproportionation of H_2O_2 by MoO_4^{2-} was investigated earlier by Aubry et al.,[26] and it is of note that the reaction kinetics are different to that observed with **1** (Figure S10). With excess H_2O_2, **1** shows a relative constant rate of $^3O_2$ evolution between 0–2500 s (Figure 3), whereas MoO_4^{2-} shows a pronounced initial lag phase, followed by a steady rate of $^3O_2$ evolution for ca. 500 s and thereafter the evolution of $^3O_2$ continues at a much lower rate until it ceases at ca. 3500 s (Figure S10). The discontinuous time dependence of $^3O_2$ evolution is due to the different rates at which the various peroxomolybdate species disproportionate H_2O_2: the oxotriperoxomolybdate ($[MoO(O_2)_3]^{2-}$) species disproportionates it 20 times faster than the dioxodiperoxomolybdate ($[MoO_2(O_2)_2]^{2-}$) and tetraperoxomolybdate ($[Mo(O_2)_4]^{2-}$).[26] This is apparent when comparing the decay

of H_2O_2 with the formation of $^3O_2$ (Figure S10): $^3O_2$ is liberated in the head space long after mostly all of the H_2O_2 has been consumed. Additionally, the stoichiometric balance of the H_2O_2:$^3O_2$ is 2:1 for **1**, but 3:2 for MoO_4^{2-} under the conditions used. It is of note that the concentration of MoO_4^{2-} gives a maximum of 6 turnovers of which 1 equivalent of H_2O_2 is used for the initial oxidation of the catalyst to the resting state. This contrasts with the much lower concentration of **1** used, which shows 400 turnovers, and the amount of H_2O_2 needed to generate the Fe(III) resting state is negligible.

The optical system was arranged such that the $^3O_2$ released into the head space of a sealed cuvette was quantified by Raman spectroscopy at 785 nm and the chemiluminescence from $^1O_2$ emitted from the reaction mixture was collected by the NIR emission spectrometer concurrently. In this way, the rate of $^3O_2$ evolution from decomposition of H_2O_2 and the chemiluminescence from $^1O_2$ over time could be correlated. The relation between chemiluminescence from $^1O_2$ generated by the catalyst Li_2MoO_4 reacting with H_2O_2 with the evolution of $^3O_2$ into the headspace is readily apparent in Figure 7A,B, which shows chemiluminescence from $^1O_2$ and $^3O_2$ evolution, respectively. Hence, despite that the concentration of OH oscillators (*i.e.* water, which quenches $^1O_2$ efficiently) introduced with the H_2O_2 is significant, the NIR emission spectrometer is capable of detecting the emission from the $^1O_2$ produced as it relaxes to $^3O_2$.

Comparison of a plot of number of moles of $^3O_2$ gas released into the headspace and intensity of NIR emission from radiative relaxation of $^1O_2$ over time (Figure 7C) with the cumulative emission intensity over time shows a near perfect overlap with the release of $^3O_2$ into the headspace. This correlation is expected since the chemiluminescence from $^1O_2$ indirectly relates to the overall rate of formation of $^3O_2$. There is, however, an offset between 1000–2000 s, which is ascribed to a lag time between the formation of $^3O_2$ in solution (i.e., considering its solubility and lack of convection) and its appearance in the head space of the cuvette at the point at which the Raman probe is focused. Importantly, Figure 7D shows the same reaction progresses at the final reaction stage in which a trend line between 4200–5000 s is determined from the $^3O_2$ curve. The rate of release of $^3O_2$ is 9.2 nmol/s in this period (note that Li_2MoO_4 produces $^1O_2$ from H_2O_2 quantitatively[24]), and shows that the limit of detection of $^1O_2$ chemiluminescence with the present optical system is sufficient to detect emission at such low photon fluxes. The rate of release of $^3O_2$ therefore serves as the lower limit of $^1O_2$ chemiluminescence detection in the H_2O_2 disproportionation by **1**.

$^1O_2$ chemiluminescence with H_2O_2 and 1

The $^1O_2$ chemiluminescence and the evolution of $^3O_2$ from the **1**/H_2O_2 system are shown in Figure 8A. Figure 8B shows the evolution of $^3O_2$ and luminescence intensity over time. In contrast to Li_2MoO_4, with **1** emission from $^1O_2$ is not observed during the disproportionation of H_2O_2. The initial rate of $^3O_2$ formation (between 250–750 s) (Figure 8B) corresponds to 158 nmol/s, which is well above the limit of detection of the system (9.2 nmol/s) and indicates that no more than 6% of $^3O_2$ that is liberated through H_2O_2 disproportionation by

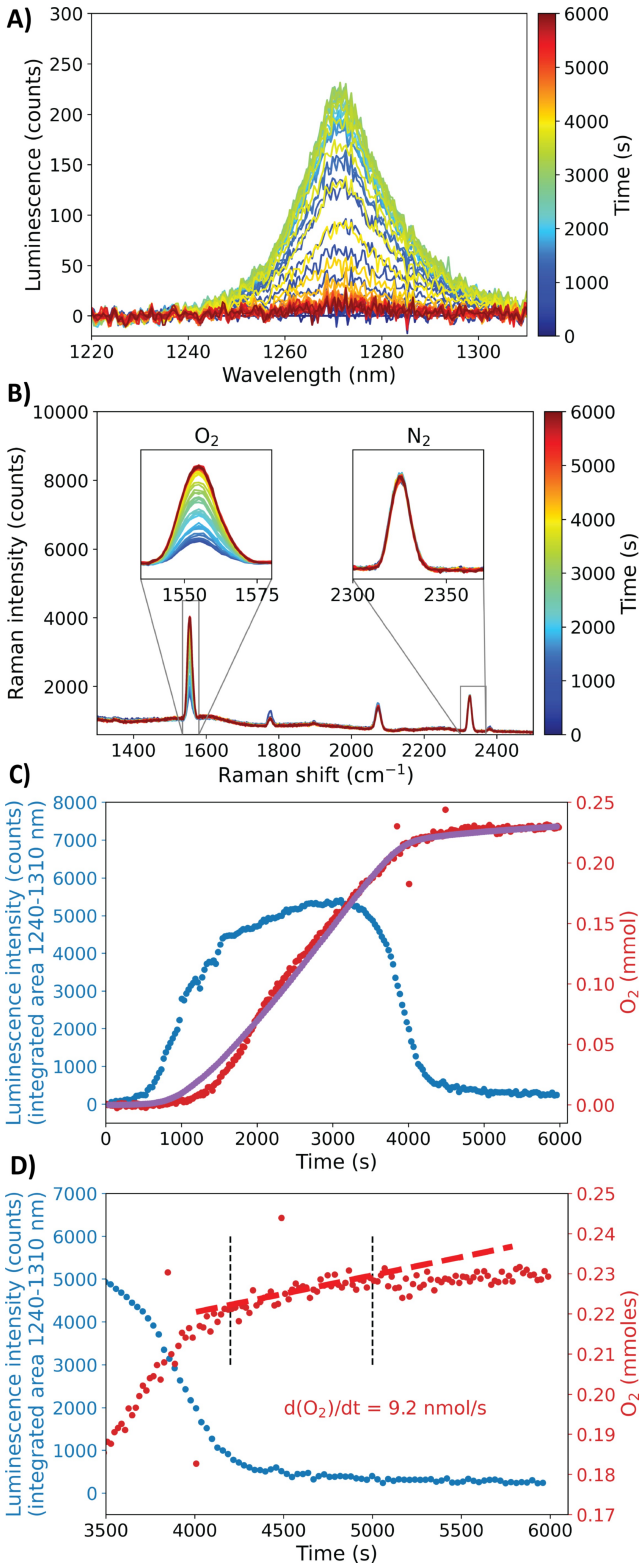

Figure 7. Chemiluminescence from $^1O_2$ and head space Raman spectroscopy during the reaction of Li_2MoO_4 with H_2O_2. A) NIR emission and B) head space Raman spectra (λ_{exc} 785 nm) over time. C) Integrated intensity of emission at 1270 nm (blue), cumulative middle Riemann sum of the $^1O_2$ chemiluminescence (purple) and number of moles of $^3O_2$ released into the head space (red) over time. D) Expansion of between 3500–6000 s from C. Conditions: 43 mM Li_2MoO_4, 263 mM H_2O_2 in CD_3OD at 19 °C.

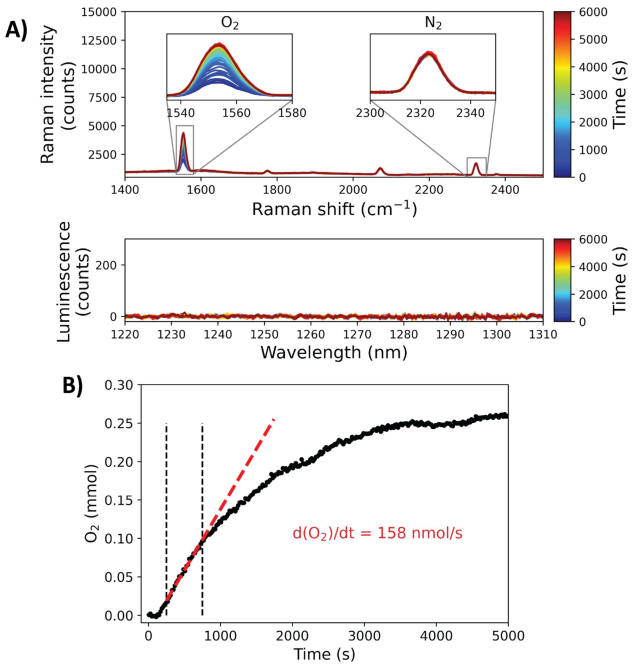

Figure 8. NIR emission spectra and head space Raman spectroscopy during the reaction of **1** with H_2O_2. A) NIR emission spectra and head space Raman spectroscopy (λ_{exc} 785 nm) over time. B) Number of moles of $^3O_2$ released into the head space over time. Conditions: 0.5 mM **1**, 275 mM H_2O_2 in CD_3OD at 19 °C.

1 may be released initially as $^1O_2$. Hence, the levels of $^1O_2$ corroborate conclusions reached from earlier DFT calculations (vide infra),[14] that only $^3O_2$ is formed in the reaction with **1**. However, an important factor to consider is that the iron complexes themselves can potentially act as a quencher for $^1O_2$.

$^1O_2$ photoluminescence with $[Ru(bipy)_3]^{2+}$

As a control, the $^1O_2$ photosensitizer $[Ru(bipy)_3]^{2+}$ was used in the presence of **1** (excitation at 450 nm) in methanol to determine how significant the quenching by **1** of $^1O_2$ luminescence is (Figures S11 and S12). Addition of **1** to $[Ru(bipy)_3]^{2+}$ in methanol decreases the intensity of $^1O_2$ luminescence due to dilution and the primary inner filter effect (**1** and **2** absorb at 450 nm). Similarly, $^1O_2$ luminescence decreased upon addition of a few equivalents of H_2O_2 due to the addition of extra OH oscillators. However, when excess H_2O_2 (400 equiv.) was added, an initial increase in emission intensity was observed due to saturation of the methanol with O_2 and thereafter the emission intensity remained constant for the remainder of the reaction, confirming that **3** does not quench $^1O_2$.

Density Functional Theory and microscopic mechanism

The reaction coordinate diagram for the reaction of **3** with H_2O_2 and energies for all products and transition states is shown in Figure 9. The first step involves concomitant homolytic cleavage of the O–O bond with hydrogen atom transfer (HAT) from H_2O_2

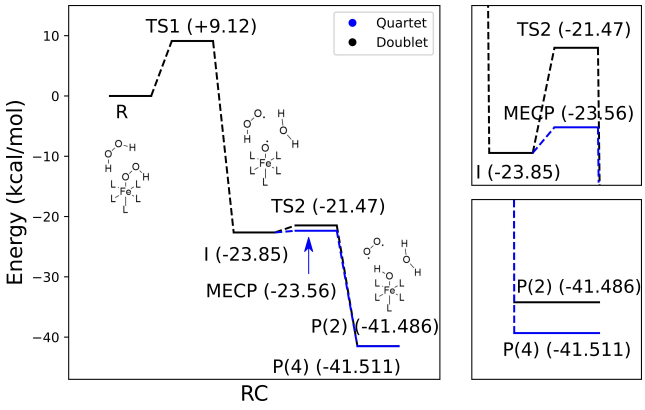

Figure 9. Reaction coordinate diagram for the reaction of **3** with H_2O_2. Relative energies compared to the reactant are given in brackets. The product energy is slightly lower for the quartet product.

to the nascent hydroxyl radical to form H_2O and HOO•. The lower initial reaction barrier and high driving force makes this mechanism overall plausible. However, in the study by Chen et al.[14] only the reaction pathway in black (in the doublet state) was considered. Inclusion of the quartet state gives a mechanism, which results in a slightly lower final energy. The two pathways considered here are (i) an adiabatic pathway to form triplet oxygen, via TS2 and (ii) a non-adiabatic pathway via an MECP (minimal energy cross point) between the doublet and quartet states. At the MECP the total spin increases from $S=\frac{1}{2}$ to $S=\frac{3}{2}$, *i.e.*, with an unpaired electron at the Fe-OH center that is coupled to two unpaired electrons on the O_2 molecule (Figure S13).

MECP versus TS2 and nature of products

A Minimal Energy Crossing Point (MECP)[33] provides a route for spin forbidden reactions to occur. They are defined as geometric points where two (or more) spin states have equal energy. The energy gap between the intermediate and the MECP, between the doublet and quartet states, is low (0.29 kcal/mol) and hence is expected to be a faster route than the non-adiabatic route. Additionally, the quartet is lower energy than the doublet product. This low MECP barrier can be understood easily as resulting from the spin-flip from β to α on the iron-oxygen moiety. The energy of the final product is significantly decreased due to the use of broken-symmetry DFT which produces a solution where the oxygen and low spin iron's electrons are ferromagnetically coupled to each other (Figure S13).

Simulation and fitting of kinetic data

The mechanism proposed earlier for the reactions of **1** with H_2O_2 (Figure 2) was simulated using known rate constants for the individual reactions.[14] The rate constants for the elementary steps involved in the catalytic disproportionation were

complemented with k_{-1}, the reverse of k_1 (Figure 10). k_{-1} was obtained by fitting of the concentration of **3** between 0–100 s with various initial equivalents of H_2O_2 (Figure 11). The best fit for k_{-1} (between 0.000 s^{-1} and 0.045 s^{-1}) is much lower than k_1, indicating that the equilibrium lies heavily towards **3**.

The concentrations of various iron species, $^3O_2$, and H_2O_2 was modelled using a microkinetic model (Figure 10), using the differential equations for the rate of change of the reaction components (iron species, $^3O_2$, and H_2O_2, etc.) as input with known rate constants (Figures S14–16). The modelled reaction progress, in terms of changes in $^3O_2$ and H_2O_2 concentrations and partial pressures for 400 equiv. H_2O_2, is compared to experimental data (Figure 12 (Top), see Figure S17 for spectral data). The modelled concentration of H_2O_2 matches well with the experimental data; however, the modelled concentrations of $^3O_2$ deviate from the experimental data in that $^3O_2$ is formed more rapidly than predicted. An explanation is that the second order rate constant for H_2O_2 disproportionation was determined from the observed rate of H_2O_2 decomposition, rather than $^3O_2$ formation.[14] The higher than predicted rate of $^3O_2$ formation hints that the "true" rate of H_2O_2 disproportionation may be somewhat greater than 0.8 M^{-1} s^{-1}.

The modelled concentration of **3** over time with 400 equiv. H_2O_2 (Figure 12 (Bottom)) shows good agreement with experimental data for the first 3000 s. Thereafter the prediction and experimental data deviate strongly, indicating that an additional decay reaction for **3**, not considered in the mechanism, is important when essentially all of the H_2O_2 has undergone disproportionation. We surmised that **3** may react with itself in a second order process.

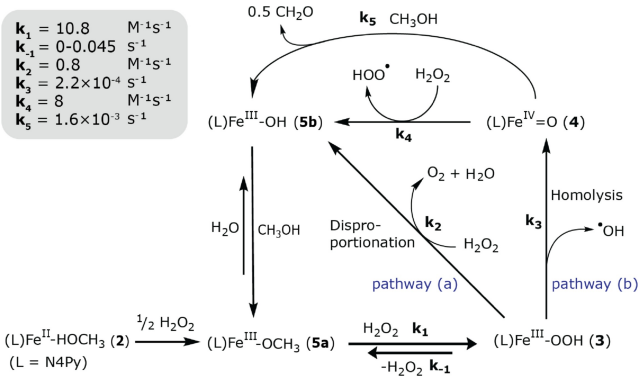

Figure 10. Proposed mechanism of **1** with excess H_2O_2 in methanol including k_{-1} and k_5. k_5 is the pseudo-first-order rate constant for the reaction of **4** with methanol.

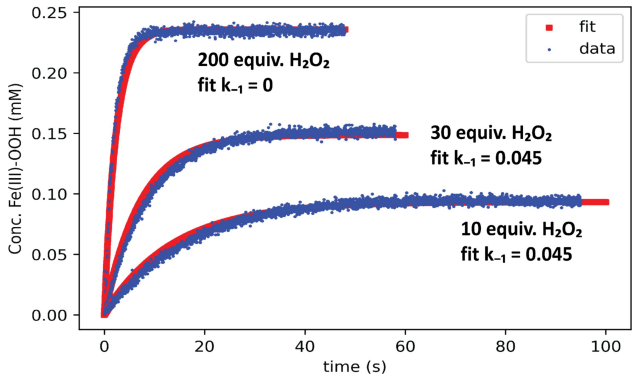

Figure 11. Fitting of k_{-1} from change in concentration of **3** over time after addition of H_2O_2. Conditions: 0.25 mM **1** and various initial concentrations of H_2O_2 (10 equiv., 30 equiv., and 200 equiv. w.r.t. **1**).

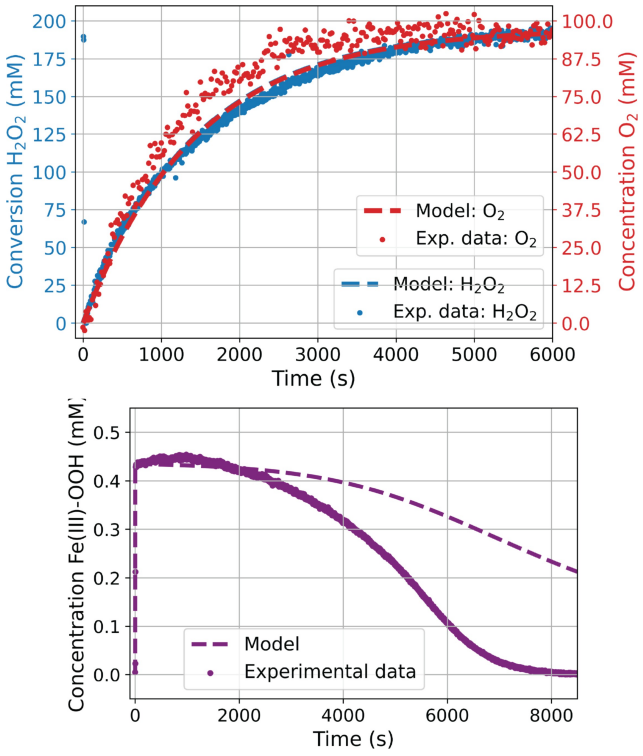

Figure 12. Experimentally determined reaction progress with the simulated progress based on model shown in Figure 10 for an initial 400 equiv. H_2O_2. Top: $^3O_2$ (red) and H_2O_2 (blue) reaction progress determined by Raman spectroscopy. Bottom: concentration of **3** over time from visible absorption spectroscopy. Conditions: 0.46 mM **1** and 190 mM H_2O_2 in methanol. Visible absorbance, head space and liquid phase Raman spectra were recorded concurrently. See Figure S17 for spectral data and further details regarding the model used.

H_2O_2 disproportionation was examined with different initial concentrations of **1** (5 mM, 1 mM, 50 μM, Figure S18–19) to explore this hypothesis. UV/vis absorption spectroscopy shows that the decay of **3** is much faster with 5 mM **1** than with 50 μM **1**, consistent with bimolecular reactivity. In Figure 13 the extra elementary step is added to the mechanism with second order rate constant k_6, estimated to be between 10 and 15 M^{-1} s^{-1}. Furthermore, the first order rate constant k_3 was determined to be greater (between 0.002 and 0.007 s^{-1}) from experiments carried out with 50 μM **1**. Here the second order process (k_6) is of less importance, and thus the first order process (k_3) may be estimated as it determines the decomposition of **3** primarily. Figure 14 shows the predicted concentrations of **3**, H_2O_2, and $^3O_2$ taking into consideration the extra elementary step (k_6) and the adjusted value of k_3. The modified model indicates that the prediction for H_2O_2 and $^3O_2$ remains accurate, and here the modelled decay of **3** approximates the experimental data better also. The estimated rate constants k_3 and k_6 are relevant for

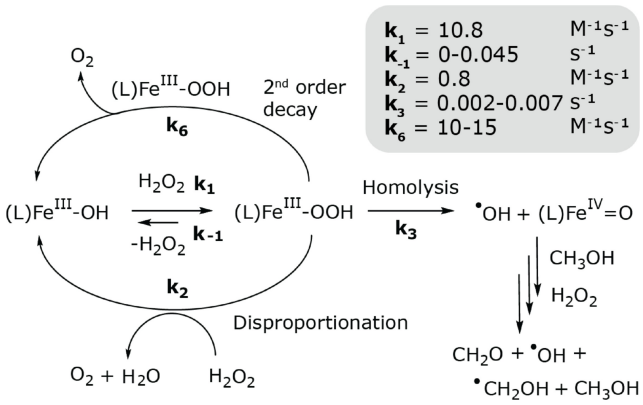

Figure 13. Proposed mechanism focused on the reactivity of the **3**, with the additional elementary step of the second order decay of **3** (k_6).

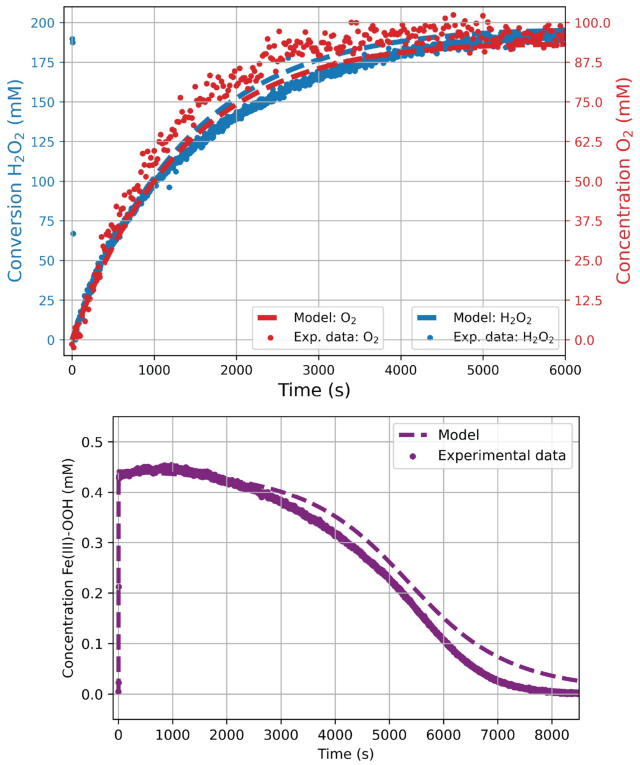

Figure 14. Reaction progress expected on basis of modified mechanism shown in Figure 13 for the conversion of 400 equiv. H_2O_2 compared with experimental data. Top: Concentration of $^3O_2$ (red) and H_2O_2 (blue) over time. Bottom: Concentration of **3** over time. Visible absorbance, and head space and liquid phase Raman spectroscopy were recorded concurrently. Conditions: 0.46 mM **1** and 190 mM H_2O_2 in methanol. See supporting information for details of model.

understanding the formation of OH radicals (through O–O bond cleavage in **3**). Figure 15 shows the relation between k_{obs} vs [**3**] for the homolytic decay (k_3) and the 2nd order decay (k_6) processes, respectively.

The concentration dependence of the two decay processes show a salient point at ca. 0.13 mM **3** where the dominant decay pathway switches, which is consistent with data shown in Figure 14 (bottom). From Figure 15 it is apparent that formation of hydroxyl radicals and **4** proceeds at a rate of ca. 1 μM/s with

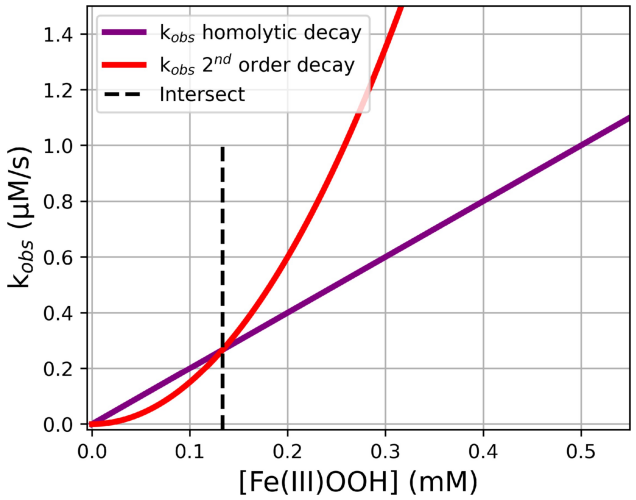

Figure 15. Relation between the observed rate, k_{obs}, and the individual decay processes for **3**; the homolytic decay, k_3 (estimated 0.002 s^{-1}), and the 2nd order decay, k_6 (estimated 15 $M^{-1}s^{-1}$).

[**3**] = 0.5 mM, which is possibly responsible for initiating auto-oxidative reactions. In methanol alone, both hydroxyl radicals and the **4** oxidise methanol to formaldehyde. From Figure 15 the amount of formaldehyde formed can be identified by determining the area under the homolytic decay pathway (purple line) between the initial concentration of **3** (ca. 0.45 mM) and its final concentration (zero). However, the 0.125 mM formaldehyde that would be formed in this case (multiplying [**3**] = 0.5 mM and k_{obs} = 1 μM/s and dividing by 2), results in >0.1% efficiency of formaldehyde formation w.r.t. H_2O_2 added (200 mM), whereas an efficiency of 2% was determined earlier for similar conditions of [H_2O_2] (800 eq).[14] This discrepancy may be rationalised if the assumption that OH radicals react with methanol stoichiometrically is false; indeed it is known that OH radicals induce chain reactions of methanol-to-formaldehyde oxidation in the presence of H_2O_2.[34,35] These radical processes were not included in the catalytic model, and are indeed difficult to model, but can be assumed to be responsible for a part of the H_2O_2 decay (HAT from H_2O_2 by hydroxyl radical to form water and superoxide) and the formation of formaldehyde also.

Discussion

The disproportionation of H_2O_2 catalysed by **1** was investigated earlier by Chen et al.,[14] from which it was confirmed by reaction monitoring that the species responsible for H_2O_2 oxidation was **3**. Initial DFT studies confirmed the energetic soundness of this conclusion, including the prediction of an intermediate formation of a hydrogen bonded superoxide radical, and predicted that the reaction would lead to the generation of $^3O_2$, but only the low-spin state was considered. In the present study the formation of $^1O_2$ was investigated using both chemical probes and by chemiluminescence. Near infrared emission spectroscopy, with the well-established singlet oxygen

generator [MoO_4^{2-}] was used as a positive control and, by ensuring the rates of disproportionation of H_2O_2 were similar under the experimental conditions employed, it was confirmed that **1** does not produce $^1O_2$ corroborating the predictions made by DFT calculations.

Revisiting the mechanism by DFT methods considering broken symmetry calculations and possible MECPs, we found here that the two step process involving a transient protonated superoxide intermediate was followed by a very low barrier for the subsequent step to form oxygen. The low barrier is consistent with the absence of reactivity of the transiently formed **4** (Fe(IV)O) H-bonded to the protonated superoxide, as they react immediately by a second HAT. It is of note that should the protonated superoxide escape **4**, it will react rapidly with methanol and this side reaction may account for some of the methanol oxidation observed. The present DFT studies also considered a minimum energy crossing point (MECP) between the doublet and quartet surfaces, which provides a second channel by which only $^3O_2$ is formed.

Although O–O bond homolysis in **3** is frequently proposed in mechanistic cycles, experiments at low concentrations of **1** confirmed that the rate constant for this reaction estimated earlier,[14] is indeed much lower than the reaction between two molecules of **3**. Hence, the release of protonated superoxide is possibly more important as a source of oxidant for methanol oxidation, in addition to the OH radical induce chain reactions.[34,35] Thus, there is a second pathway to methanol oxidation besides pathway b (Figure 10), *i.e.*, via **4** and an hydroxyl radical. An unexpected observation made in efforts to establish the generation of $^1O_2$ using chemical probes was that under such conditions $^3O_2$ was consumed from, rather than released, into the headspace during disproportionation. While it would be expected that the trapping of $^1O_2$ would reduce the amount of oxygen released into the headspace, it should not lead to a consumption of $^3O_2$. Product analysis confirmed that the oxygen consumption was due to auto-oxidation solely. These data indicate that sufficient free radicals are generated during disproportionation, which combined with the saturation of the solution with $^3O_2$, creates an ideal condition for auto-oxidation. This observation prompted us to consider the origin of these radicals, *e.g.*, do they arise from O–O bond homolysis in **3**.

Using the available data, we constructed a microkinetic model based on the mechanism shown in Figure 2 to establish the significance of pathway b (O–O bond homolysis) overall and thereby the origin of oxidation products of methanol. The rate constants for the reaction of **3** with H_2O_2 and with itself are order of magnitudes larger compared to O–O bond homolysis in **3**. This implies that **4** does not form in significant amounts at high [H_2O_2], and hence it is only available as the [H_2O_2] becomes negligible. This together with the knowledge that **4** reacts rapidly with (protonated) superoxide and H_2O_2 rapidly raises the question whether **4** plays any role in the oxidation of organic substrates under these conditions.

In probing the reaction for $^1O_2$ formation using Raman spectroscopy, it became clear that H_2O_2 decomposition generates sufficient free radicals to trigger autooxidation. This shows the importance of keeping a low [H_2O_2] not only to limit disproportionation but also to prevent build up of O_2 and hence radical initated autooxidation. The **1**-catalysed disproportionation of excess H_2O_2 is a wasteful reaction in regard to efficiency of organic oxidation reactions but further than that, the generation of reactive oxygen species needs to be considered also. Protonated superoxide and hydroxy radicals are likely to be primarily responsible for reactions with organic substrates here.

Conclusions

While formation of $^1O_2$ by H_2O_2 disproportionation can be excluded both empirically and by DFT studies, the significance of radical pathways was established, which are promoted by the presence of the oxygen formed. These radical pathways are concluded to be of greater importance than direct oxidation of organic substrates by **4** ([$(N_4Py)Fe(IV)=O]^{2+}$). Although the present investigation has focused on reactions in methanol, the solvent plays only a modest role in the disproportionation reactions, *e.g.*, in regard to H-bonding etc., and as a substrate for reactive oxygen species. Hence, the observation that **4** is unlikely to be formed from **3** ($((N_4Py)Fe(III)OOH]^{2+}$) raises questions in regard to the benefit of using low steady state concentrations of H_2O_2 to circumvent wasteful disproportionation, except perhaps where the substrate can interact with complexes equivalent to **3** as shown by Nam and coworkers with the complex $[Fe(II)(12-TMC)(CH_3CN)_2]^{2+}$.[10]

Experimental

Materials

Solvents, H_2O_2 (50 vol%), and reagents were obtained from commercial sources and used as received (H_2O_2 from Sigma Aldrich). Solvents for spectroscopic studies were spectrophotometric grade. [$(N_4Py)Fe(II)(CH_3CN)](ClO_4)_2$ (**1**) was available from earlier studies.[14]

Physical methods

NMR spectra were recorded on a Bruker 400 MHz spectrometer. UV/vis absorption spectra were recorded on a Specord600 (AnalytikJena) or Specord210plus spectrometer in 1 cm pathlength quartz cuvettes unless stated otherwise. Raman spectra at 785 nm were recorded with excitation by an ONDAX Mini-Benchtop Stabilized Laser at 785 (500 mW at source) or a Cobolt 08-NLDM (500 mW at source) coupled with a 100 micron multimode optical fibre to a Raman probe (Avantes). The Raman scattering was collected by the probe and passed by a round to line bundel optical fibre to the Shamrock163i spectrograph with a 600 l/mm 830 nm blazed grating and a idus-420-BEX2-DD CCD camera (Andor Technology). Raman spectra at 1064 nm were recorded with a 500 mW fibre coupled 1064 nm CW laser (Cobolt lasers) terminated with a collimation lens and directed into the optical path of the spectrometer with a 45° long pass dichroic beamsplitter and focused onto the sample with a 35 mm focal length 25 mm diameter lens. Raman scattering was collected by the same lens

and pass through the dichroic beamsplitter and a long pass filter (1064 nm, Semrock) to reject Rayleigh scattering and focused with a 35 mm focal length planoconvex lens into a Shamrock 193i spectrograph equipped with a idus-InGaAs diode array (Andor Technology) with a 860 nm blazed 300 l/mm grating. Raman spectra at 532 nm were recorded using a 300 mW laser (Samba, Cobolt lasers) in 180 ° backscattering geometry. A 45° long pass dichroic mirror directed the laser into the optical axis of the spectrometer. The laser was focused and Raman scatttering collected with a 7.5 cm planconvex lens. The collimated Raman scattering pass through the dichroic and a long pass filter before being focused by a 7.5 cm planconvex lens into a Shamrock300i spectrograph equipped with a 1200 l/mm grating blazed at 500 nm and a Newton EMCCD-DU970 camera (Andor Technology). The slit width was set to 50 μm. Spectra were acquired with Andor Solis with spectral calibration with cyclohexane (ASTM E 1840). Spectra were typically 0.1 to 1 s acquisitions and 10 accumulations.

Density Functional Theory

The S12 g functional together with the TZ2P basis set in ADF/QUILD/AMS 2022 was used for all optimizations, frequency calculations and MECP optimizations. Broken symmetry DFT was used for quartet states, where the spin was flipped between the iron center and the molecular oxygen.

Oxygen quantification by head space operando Raman spectroscopy

Quantification of $^3O_2$ in the head space of a closed cuvette by Raman spectroscopy requires consideration of the optical arrangement of the spectrometer system used and in particular the overlap of the confocal volume (volume of space from which Raman scattering is collected by the Raman probe optics), with the internal volume of the cuvette, as the confocal depth can exceed the depth of the cuvette. This overlap was determined by recording Raman spectra from the headspace of a cuvette before and after purging with argon (see SI for details, Figure S2). Considering a sealed cuvette (5.07 mL volume), in which 1.5 mL is liquid phase consisting of methanol (1.5 mL, solvent), H_2O_2 (17 μL, 200 mM, 50 wt% (aqueous)), **1** (0.5 mM, by addition of 0.375 mL of a 2 mM solution of the complex in MeOH) at 19 °C. The final volume of the headspace above the reaction mixture was 3.57 mL. Although disproportionation takes place in the liquid phase, the maximum solubility of $^3O_2$ in methanol is exceeded rapidly (see SI) and it is released essentially quantitatively into the headspace. The compositions of the reaction mixture and the headspace were monitored by Raman spectroscopy simultaneously with two probes. One Raman probe (λ_{785}) was focused at the head space to monitor the change in Raman scattering intensity from $^3O_2$ (1555 cm^{-1}) and N_2 (2329 cm^{-1}). A second Raman probe (λ_{785}) was focused at the liquid phase to monitor conversion of H_2O_2 through the decay in the intensity of O–O stretch band of the H_2O_2 (872 cm^{-1}). The oxygen liberated during the reaction was calculated from the Raman data obtained.

In our earlier report on the disproportionation of H_2O_2 by **1** in methanol,[14] we noted an incomplete mass balance with 28% of the H_2O_2 accounted for by disproportionation to H_2O and $^3O_2$ and only 2% of H_2O_2 used in the oxidation of methanol to formaldehyde (*i.e.*the oxidation product of the reaction of methanol with, *e.g.*, **4** and/or hydroxyl radicals). Hence, ca. 70% of the H_2O_2 was unaccounted for. We revisited the experiment here and determined that the incomplete mass balance was due to an error in the method of calculation used earlier together with unaccounted for contributions from Raman scattering from air in the the part of the confocal volume outside of the cuvette (see SI for details). Reanalysis of earlier data, and repeat of those experiments here, confirms that the mass balanced was 99% +/−3% with regard to H_2O_2 and hence greater >95% is disproportionated to H_2O and $^3O_2$ as was concluded earlier. The formula (Equation 1) to quantify the $^3O_2$ liberated from the reaction mixture into the headspace of the closed cuvette and the method used to calculate the concentration of $^3O_2$ inside the head space and solution is discussed in detail in Section 1 in the supporting information).

$$\begin{aligned}&\text{Number of moles of liberated } O_2 = n_{O_2} = \\ &\quad (\text{Raman Integral Ratio} - 1) \times \\ &\quad (p_{O_2,i}[P_a] \times V_H[m^3] \times \tfrac{1}{RT_i}\left[\tfrac{mol}{P_a \times m^3}\right] + \\ &\quad C_{O_2,i}\left[\tfrac{m^3}{m^3}\right] \times V_L[m^3] \times \tfrac{1}{V_{m,O_2}}\left[\tfrac{mol}{m^3}\right])\end{aligned} \quad (1)$$

Where $p_{O_2,i}$, initial partial pressure of $^3O_2$, V_H, volume of the head space of the cuvette, R, gas constant, T, temperature, $C_{O_2,i}$, initial solubility of $^3O_2$ in methanol, V_L, volume of the liquid inside the cuvette, and V_{m,O_2}, the molar volume of $^3O_2$.

The area underneath the $\nu_{OO\ str}$ band of $^3O_2$, after purging the cuvette with argon, was subtracted from the area with air, both normalised to the Raman band of N_2. The ratio between these corrected areas was used as the starting point for the quantification (Equation 1). It should be noted that the contribution of $^3O_2$ outside the cuvette to the Raman scattering collected is that the intensity of the Raman band will always be above the limit of detection/quantification. The area of a Raman band is linearly proportional to the partial pressure and therefore the increase in the number of moles of $^3O_2$ in the head space (Equation 1). The overall increase in gas pressure increases the solubility of $^3O_2$ in the methanol, which can be calculated using Henry's law. Hence, the increase the overall amount of $^3O_2$ inside the cuvette is the sum of the increase in $^3O_2$ in the head space and the increase of dissolved $^3O_2$ in the methanol (Equation 1).

$^1O_2$ trapping experiments

Reaction with 1 at 22% conversion of α-terpinene

An empty cuvette was purged with argon and a spectrum recorded at 532 nm to determine Raman scattering intensity originating from inside and outside of the cuvette. Then, the cuvette was air-equilibrated and 0.122 mL α-terpinene (0.75 mmol, 0.5 M) and 14 μL 50% H_2O_2 (aq.) (0.25 mmol, 166 mM H_2O_2) were added to 1.26 mL of methanol. 0.5 mM **1** (by addition of 0.100 mL of a solution of 2.6 mg **1** in 0.5 mL methanol) was added to the cuvette to initiate the reaction and Raman spectra were recorded over 3700 s (at 532 nm head space: a series of 185 spectra with 2 s acquisition and 10 accumulations per spectrum; at 1064 nm liquid phase: a series of 250 spectra with 5 s acquisition and 4 accumulations per spectrum).

Reaction with 1 at 50% conversion of α-terpinene

A solution of 1.26 mL methanol, 0.122 mL α-terpinene (0.75 mmol, 0.5 M) and 42.6 μL 50% H_2O_2 (aq.) (0.75 mmol, 0.5 M H_2O_2) was prepared. The ^{1}H-NMR spectrum of a sample was recorded. 0.5 mM **1** (added as 0.1 mL of a stock solution of 2.6 mg **1** in 0.5 mL methanol) was added to the cuvette to initiate the reaction and Raman spectra were recorded over 7200s (at 785 nm for the liquid

phase: a series of 360 spectra with 1 s acquisition time and 20 accumulations per spectrum). A sample was withdrawn for ^{1}H-NMR spectral analysis.

Reaction with α-terpinene with H_2O_2 and Li_2MoO_4

A solution of 1.21 mL methanol, 0.122 mL α-terpinene (0.75 mmol, 0.5 M) and 26 mg (0.15 mmol, 0.1 M) Li_2MoO_4 was prepared. A sample for ^{1}H-NMR spectroscopy was recorded. 170 μL 50% H_2O_2 (aq.) (3 mmol, 2 M H_2O_2) was added in portions to the cuvette (3 portions, 56.7 μL each; after 0 h, 1 h and 1.5 h). Raman spectra were recorded over 7200 s (at 785 nm for the liquid phase: a series of 360 spectra with 1 s acquisition time and 20 accumulations per spectrum). A sample was withdrawn for ^{1}H-NMR spectral analysis.

NIR emission spectroscopy

$^1O_2$ emission spectra were recorded using a spectrometer optimized for Raman spectroscopy at λ_{exc}1064 nm (see experimental section "physical methods" for details). The spectrograph slit width was 10 μm for Raman spectroscopy and 25 μm for emission spectroscopy. The collection path was optimized using Raman scatter from cyclohexane, and spectra were calibrated using cyclohexane (ASTM E 1840). Reference spectra for $^1O_2$ emission were recorded using $[Ru(bipy)_3]^{2+}$ with excitation at 450 nm (35 mW) directed to follow the collection path using a dichroic mirror (DMPL900, Thorlabs).

A Raman probe (λ_{785}) focused on the head space of the cuvette equipped with a screw cap and septum holding the reaction mixture. Experiments with **1** were conducted with **1** (0.5 mM, added as 0.5 mL of a 1.5 mM **1** solution in CD_3OD) with an additional 1 mL CD_3OD. H_2O_2 (275 mM, 23 μL 50 wt% H_2O_2 in H_2O added) was added through the septum of the cuvette by syringe to initiate the reaction. For experiments with MoO_4^{2-}, Li_2MoO_4 (43 mM, 16.5 mg) was added to 1.59 mL CD_3OD, followed by H_2O_2 (263 mM, 23 μL 50 wt% H_2O_2 in H_2O added by syringe) to initiate the reaction.

A control experiment to determine potential interference of **1** and its oxidation products with the luminescence of $^1O_2$ emission was carried out using the oxygen sensitiser $[Ru(bipy)_3]^{2+}$ with excitation at 450 nm (35 mW). A solution of 30 μM $[Ru(bipy)_3]^{2+}$ in methanol was prepared (A = 1.73 at λ_{max} = 285 nm) from which 1.05 mL was added to a cuvette. 0.15 mL of a 5 mM **1** solution in methanol was added to the cuvette to obtain 0.65 mM **1** and 27 μM $[Ru(bipy)_3]^{2+}$ in 1.2 mL methanol and a luminescence spectrum was recorded. Ca. 3 equiv. H_2O_2 w.r.t. **1** (2.2 mM H_2O_2, added as 3 μL of a 883 mM H_2O_2 solution in methanol) was added to the solution to convert to a and another luminescence spectrum was recorded. Consequently, H_2O_2 (177 mM, added as 0.3 mL of a 883 mM H_2O_2 solution in methanol) was added to the solution and the emission spectrum was monitored over 2 h. The final concentrations were 21 μM $[Ru(bipy)_3]^{2+}$, 0.5 mM **1**, and 177 mM H_2O_2 in 1.5 mL methanol. Head space Raman spectra (λ_{785}) were recorded before and after addition of excess (177 mM) H_2O_2.

Computational studies

Computational studies were performed using ADF[36] and QUILD,35[37,38] as reported earlier.[14] Briefly, geometry optimization and frequency calculations were performed using the unrestricted density functional S12 g spin-state consistent functional[39,40] with a triple-ζ valence plus double polarization (TZ2P) basis set. Free energy (ΔG) corrections, thermal and entropic corrections were made from frequency calculations at 298 K. The solvation energy was considered using methanol as a solvent with the COSMO solvation model as implemented in ADF.[41] A VeryGood grid was used for all calculations, except for the frequency calculations which were run with a Normal grid. Scalar relativistic corrections have been included self-consistently in all calculations by using the zeroth-order regular approximation (ZORA).[42] All DFT calculations were performed using the unrestricted Kohn-Sham scheme.

Numerical simulation of the catalytic decomposition of H_2O_2

Numerical simulation was performed in Python using the "odeint" module from the "scipy.integrate" package. The set of elementary reaction steps with corresponding differential equations of the species involved, as well as the python script, are reported as supporting information. The **3**, H_2O_2, and $^3O_2$ were quantified from experimental data as follows: [**3**] was estimated from the absorbance at 550 nm (ε = 1100 M^- cm^{-1}), H_2O_2 from Raman spectra using a calibration curve (Figure S18), and $^3O_2$ via the quantification method described earlier.

Reactions with 1 (0.25 mM)

A solution of 0.25 mM **1** in 2 mL methanol (added as 1 mL of a 0.5 mM **1** solution in methanol) was added to a cuvette. While recording UV/visible absorption (Specord600), 10 equiv. H_2O_2 (added as 28 μL 176 mM H_2O_2), 30 equiv. H_2O_2 (added as 8.5 μL 1.8 M H_2O_2), or 200 equiv. H_2O_2 (added as 57 μL 1.8 M H_2O_2) was added.

Reaction with 1 (0.5 mM) concurrently monitored by Raman (head space and liquid phase) and UV/vis absorption spectroscopy

A solution of 0.5 mM **1** in 1.1 mL methanol (added as 0.3 mL of a 5 mM **1** solution in methanol) was added to a 1 cm path length cuvette with screw-cap and septum. While recording UV/visible absorption (home setup, using an Avantes spectrometer and lightsource), and headspace and liquid phase Raman spectra at 785 nm, H_2O_2 (194 mM, added as 0.4 mL of a 710 mM H_2O_2 solution in methanol) was added through the septum to the cuvette. The reaction was monitored over 2 h. Head space Raman scattering were corrected for air in the part of the confocal volume outside of the cuvette as described before.

Similarly, reactions were performed with different amounts of H_2O_2: for 100, 50, 20, and 5 equiv. H_2O_2, respectively 0.1 mL, 50 μL, 20 μL, and 5 μL of a 710 mM H_2O_2 solution in methanol was added to a solution containing 0.5 mM **1** (added as 0.3 mL of a 5 mM **1** solution in methanol), where different amounts of methanol were added to result in a 1.5 mL total volume.

Reaction with 1 (50 μM)

A solution of 50 μM **1** in 19.6 mL methanol (added as 0.2 mL of a 5 mM **1** solution in methanol) was added to a 10 cm path length cuvette. While measuring UV/visible absorption, H_2O_2 (18 mM, added as 0.4 mL of a 883 mM H_2O_2 solution in methanol) was added as evenly as possible over the length of the 10 cm path length cuvette and the solution was mixed by pipetting in and out the solution. The UV/vis absorption spectra were recorded over 3 h.

Reaction with 1 (1 mM)

A solution of 1 mM **1** in 0.9 mL methanol (added as 0.3 mL of a 5 mM **1** solution in methanol) was added to a 1 cm path length cuvette. While measuring UV/vis absorption, H_2O_2 (350 mM, added

as 0.6 mL of a 883 mM H_2O_2 solution in methanol) was added as evenly as possible over the length of the 10 cm path length cuvette and the solution was mixed by pipetting in and out the solution. The UV/vis absorption spectra were recorded over 2 h.

Reaction with 1 (5 mM)

A solution of 5 mM **1** in 0.5 mL methanol was added to a 2 mm path length cuvette. While measuring UV/vis absorption spectra, H_2O_2 (90 mM, added as 0.057 mL 50 wt% H_2O_2 (aq.)) was to the 2 mm path length cuvette and the solution was mixed by pipetting in and out the solution. The UV/vis absorption spectra were recorded over 2 h.

Acknowledgements

This work is part of the Advanced Research Center for Chemical Building Blocks, ARC CBBC, which is co-founded and co-financed by the Dutch Research Council (NWO) and the Netherlands Ministry of Economic Affairs and Climate Policy (ARC-CBBC, 2021.038C.RUG.8). AEI/MCIN, Grant: PID2020-114548GB–I00; GenCat, Grant: 2021SGR00487; SCM: developer's license to M.S.

Conflict of Interests

The authors have no conflicts of interest to declare.

Data Availability Statement

The data that support the findings of this study are available from the corresponding author upon reasonable request.

Keywords: iron · singlet oxygen · hydrogen peroxide · catalase · mechanism

[1] F. Lledias, W. Hansberg, *Photochem. Photobiol.* **1999**, *70*, 887.
[2] J. T. Groves, R. C. Haushalter, M. Nakamura, T. E. Nemo, B. J. Evans, *J. Am. Chem. Soc.* **1981**, *103*, 2884.
[3] P. Jones, H. B. Dunford, *J. Inorg. Biochem.* **2005**, *99*, 2292.
[4] M. Lubben, A. Meetsma, E. C. Wilkinson, B. L. Feringa, L. Que, *Angew. Chem. IE* **1995**, *34*, 1512.
[5] G. Roelfes, M. Lubben, K. Chen, R. Y. N. Ho, A. Meetsma, S. Genseberger, R. M. Hermant, R. Hage, S. K. Mandal, V. G. Young, Y. Zang, H. Kooijman, A. L. Spek, L. Que, B. L. Feringa, *Inorg. Chem.* **1999**, *38*, 1929.
[6] D. Kumar, H. Hirao, L. Que, S. Shaik, *J. Am. Chem. Soc.* **2005**, *127*, 8026.
[7] K.-B. Cho, X. Wu, Y.-M. Lee, Y. H. Kwon, S. Shaik, W. Nam, *J. Am. Chem. Soc.* **2012**, *134*, 20222.
[8] M. Borrell, E. Andris, R. Navrátil, J. Roithová, M. Costas, *Nat. Commun.* **2019**, page 901.
[9] S. Xu, A. Draksharapu, W. Rasheed, L. Que, *J. Am. Chem. Soc.* **2019**, *141*, 16093.
[10] W. Zhu, A. Kumar, J. Xiong, M. J. Abernathy, X.-X. Li, M. S. Seo, Y.-M. Lee, R. Sarangi, Y. Guo, W. Nam, *J. Am. Chem. Soc.* **2023**, *145*, 4389.
[11] W. N. Oloo, M. Szávuly, J. Kaizer, L. Que, *Inorg. Chem.* **2022**, *61*, 37.
[12] J.-N. Rebilly, C. Herrero, K. Sénéchal-David, R. Guillot, T. Inceoglu, H. Maisonneuve, F. Banse, *Chem. Sci.* **2021**, *12*, 15691.
[13] A. Bohn, C. Chinaux-Chaix, K. Cheaib, R. Guillot, C. Herrero, K. Sénéchal-David, J.-N. Rebilly, F. Banse, *Dalton Trans.* **2019**, *48*, 17045.
[14] J. Chen, A. Draksharapu, D. Angelone, D. Unjaroen, S. K. Padamati, R. Hage, M. Swart, C. Duboc, W. R. Browne, *ACS Catal.* **2018**, *8*, 9665.
[15] G. Roelfes, M. Lubben, R. Hage, L. Que, Jr., B. L. Feringa, *Chem. Eur. J.* **2000**, *6*, 2152.
[16] J. Kaizer, E. J. Klinker, N. Y. Oh, J.-U. Rohde, W. J. Song, A. Stubna, J. Kim, E. Münck, W. Nam, L. Que, *J. Am. Chem. Soc.* **2004**, *126*, 472.
[17] F. Thorning, P. Henke, P. R. Ogilby, *J. Am. Chem. Soc.* **2022**, *144*, 10902.
[18] M. Bregnhøj, M. Westberg, F. Jensen, P. R. Ogilby, *Phys. Chem. Chem. Phys.* **2016**, *18*, 22946.
[19] T. Yang, J. Choo, S. Stavrakis, A. de Mello, *Chem. Eur. J.* **2018**, *24*, 12078.
[20] M. Orfanopoulos, *Photochem. Photobiol.* **2021**, *97*, 1182.
[21] K. N. Ingenbosch, S. Quint, M. Dyllick-Brenzinger, D. S. Wunschik, J. Kiebist, P. Süss, U. Liebelt, R. Zuhse, U. Menyes, K. Scheibner, C. Mayer, K. Opwis, J. S. Gutmann, K. Hoffmann-Jacobsen, *ChemBioChem* **2021**, *22*, 398.
[22] J. Rudback, M. A. Bergstrom, A. Borje, U. Nilsson, A. T. Karlberg, *Chem. Res. Toxicol.* **2012**, *25*, 713.
[23] J. M. Aubry, *J. Am. Chem. Soc.* **1985**, *107*, 5844.
[24] J. M. Aubry, B. Cazin, *Inorg. Chem.* **1988**, *27*, 2013.
[25] J. M. Aubry, B. Cazin, F. Duprat, *J. Org. Chem.* **1989**, *54*, 726.
[26] V. Nardello, J. Marko, G. Vermeersch, J. M. Aubry, *Inorg. Chem.* **1995**, *34*, 4950.
[27] V. Nardello, S. Bogaert, P. L. Alsters, J.-M. Aubry, *Tetrahedron Lett.* **2002**, *43*, 8731.
[28] P. L. Alsters, W. Jary, V. Nardello-Rataj, J.-M. Aubry, *Org. Process Res. Dev.* **2010**, *14*, 259.
[29] F. van Laar, D. De Vos, D. Vanoppen, B. Sels, P. A. Jacobs, A. Del-Guerzo, F. Pierard, A. Kirsch-DeMesmaeker, *Chem. Commun.* **1998**, 267–268.
[30] M. Elsherbini, R. K. Allemann, T. Wirth, *Chem. Eur. J.* **2019**, *25*, 12486.
[31] W. Adam, D. V. Kazakov, V. P. Kazakov, *Chem. Rev.* **2005**, *105*, 3371.
[32] K. Bohme, H. D. Brauer, *Inorg. Chem.* **1992**, *31*, 3468.
[33] J. N. Harvey, *WIREs Comput. Mol. Sci.* **2014**, *4*, 1.
[34] P. Ulanski, C. Von Sonntag, *J. Chem. Soc. Perkin Trans. 2* **1999**, 165–168.
[35] B. C. Gilbert, R. O. C. Norman, R. C. Sealy, *J. Chem. Soc. Perkin Trans. 2* **1974**, 824–830.
[36] E. J. Baerends, *ADF 20016.01; SCM: Amsterdam* **2016**.
[37] G. Te Velde, F. M. Bickelhaupt, E. J. Baerends, C. Fonseca Guerra, S. J. A. Van Gisbergen, J. G. Snijders, T. Ziegler, *J. Comput. Chem.* **2001**, *22*, 931.
[38] M. Swart, F. M. Bickelhaupt, *J. Comput. Chem.* **2008**, *29*, 724.
[39] M. Swart, *Chem. Phys. Lett.* **2013**, *580*, 166.
[40] M. Swart, M. Gruden, *Acc. Chem. Res.* **2016**, *49*, 2690.
[41] M. Swart, E. Rösler, F. M. Bickelhaupt, *Eur. J. Inorg. Chem.* **2007**, *2007*, 3646.
[42] E. V. Lenthe, E. J. Baerends, J. G. Snijders, *J. Chem. Phys.* **1993**, *99*, 4597.

Manuscript received: December 3, 2023
Revised manuscript received: February 4, 2024
Accepted manuscript online: February 8, 2024
Version of record online: ■■, ■■

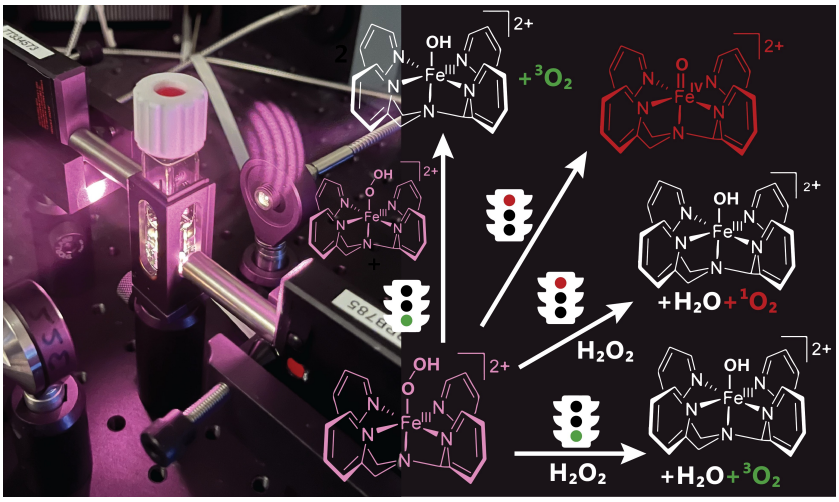

Catalytic decomposition of H_2O_2 by an iron catalyst is shown to via a Fe-(III)OOH intermediate. Surprisingly the expected homolysis of the O–O bound to yield Fe(IV)=O species does not occur significantly and oxidation products are due to radical chain reactions.

C. Maurits de Roo, A. S. Sardjan, R. Postmus, Prof. Dr. M. Swart, Prof. Dr. R. Hage, Prof. Dr. W. R. Browne**

Reaction of (N4Py)Fe with H_2O_2 and the relevance of its Fe(IV)=O species during and after H_2O_2 disproportionation